Macromolecular Rapid Communications
www.mrc-journal.de

Antimicrobial Silicon Rubber Crosslinked with Bornyl-Siloxane

Chen Chen, Songtao Wang, Xinyu Chen, Zixu Xie, Pengfei Zhang, Fanqiang Bu, Lifei Huang, Dongdong Zhao, Yuanhang Wang, Fang Liu, Wensheng Xie, Guofeng Li, and Xing Wang**

Silicone rubber (SiR) has a wide range of medical applications, but it lacks antimicrobial properties, leading to potential infection issues with related implants or medical devices. Most studies focus on adding anti-bacterial agents or surface modification, which usually result in composites with anti-bacterial properties, rather than synthesizing SiR with intrinsically antimicrobial performances. To tackle this issue, a double substituted bornyl-siloxane crosslinker (BC) is designed. This crosslinker can react with hydroxy-terminated polydimethylsiloxane (PDMS) at room temperature to yield SiR with borneol side groups. The process is simple without using additional solvents. Antimicrobial assay on SiR cured with different ratios of BC/PDMS showed that 20 wt.% BC cross-linked network exhibited outstanding anti-bacterial adhesion (*Escherichia coli* 99.4%, *Staphylococcus aureus* 97.3%) performance and long-lasting anti-mold (*Aspergillus niger* over 99% for 30 days) adhesion properties. Moreover, the subcutaneous implantation model in mice demonstrated its excellent anti-infection, biocompatibility and safety. Therefore, this material is promising for widespread adoption in the medical field, especially in silicon-based products or coatings.

1. Introduction

Infections related to medical devices and implants have become a severe issue, as some microbes adhere to those materials' surfaces, proliferate, and even form biofilms. Biofilms protect microbes from antibiotics and the host immune system, leading to persistent infections.[1] This results in prolonged hospital stays for patients, increased medical costs,[2] and in severe cases, further infections and death,[3] significantly threatening patient health.[4] In the world, it is reported that 60% of infections are caused by implants and medical devices,[5] and 80% of them are caused by biofilms on the surfaces of medical devices.[6] Therefore, addressing microbial infections on the surfaces of medical devices has become a matter of urgency.

Silicone rubber (SiR), renowned for its remarkable properties like biocompatibility,[7] stability,[8] and low toxicity,[9] has widespread usage in the medical field,[10,11] including applications such as catheters,[12] prosthetics,[13] and infusion tubes.[14] However, conventional SiR are deficient in antimicrobial adhesion capabilities,[15] rendering surfaces susceptible to microbial colonization, potentially compromising therapeutic efficacy or precipitating secondary infections.[16] To tackle these challenges, numerous antimicrobial strategies have been devised. Current research on the antibacterial modification of SiR predominantly focuses on adding antimicrobial agents to SiR or modifying the coating on its surface[17] These strategies provide SiR with significant added value and substantially broaden its antimicrobial application.[18–21] Since the grafting strategies often necessitate additional processing of the finalized SiR to establish antimicrobial surfaces, the complexity of these processes may limit their application. More importantly, research on SiR modification to resist mold adhesion is often overlooked. Mold contamination also poses a more complex challenge for treatment. This issue is further exacerbated by the limited availability of anti-mold treatments compared to antibacterial options in clinical settings.[22,23] Hence, SiR that effectively repels both bacterial and mold adhesion holds considerable promise in the biomedical realm.

In recent years, antimicrobial adhesion strategies grounded in stereochemistry have garnered growing interest among researchers. These strategies principally leverage distinct stereochemical configurations to impede the active adhesion of microbes to material surfaces, with terpenoids such as borneol and menthol emerging as the prominent antimicrobial

C. Chen, S. Wang, X. Chen, Z. Xie, P. Zhang, F. Bu, L. Huang, D. Zhao, Y. Wang, W. Xie, G. Li, X. Wang
State Key Laboratory of Organic-Inorganic Composites
Beijing Laboratory of Biomedical Materials
College of Life Science and Technology
Beijing University of Chemical Technology
Beijing 100029, P. R. China
E-mail: ligf@mail.buct.edu.cn; wangxing@mail.buct.edu.cn
F. Liu
Department of Oncology of Integrative Chinese and Western Medicine
China-Japan Friendship Hospital
Beijing 100029, P. R. China

The ORCID identification number(s) for the author(s) of this article can be found under https://doi.org/10.1002/marc.202400930

DOI: 10.1002/marc.202400930

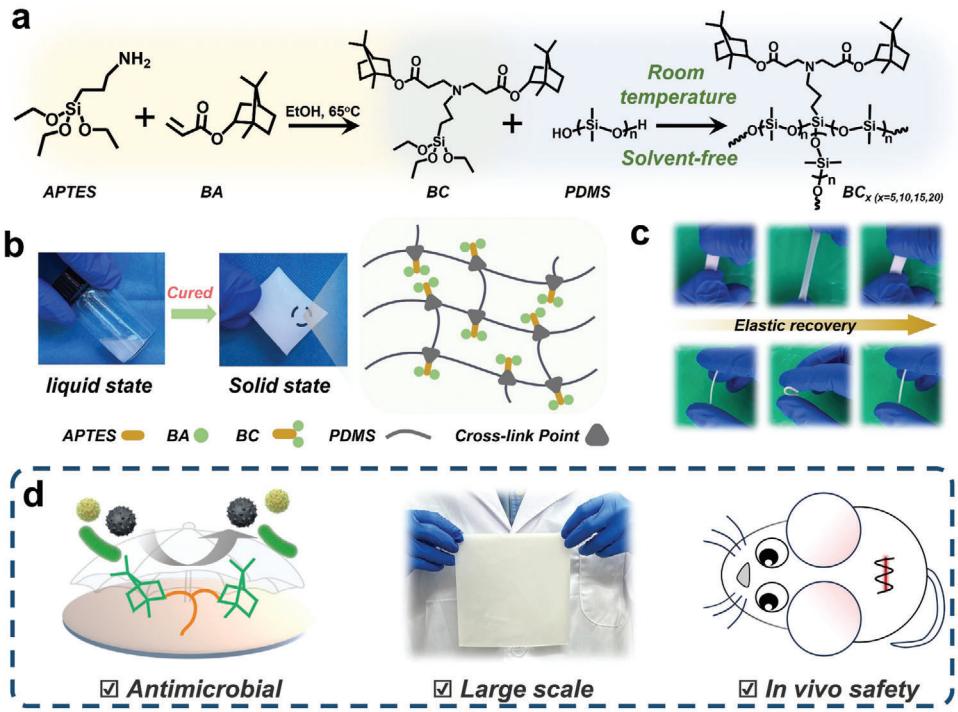

Scheme 1. Schematic diagram for the preparation of BC SiR and its advantages. a) Synthesis process of BC SiR. b) Curing process and cross-linking network schematic. c) Stretching and bending process. d) Schematic diagram of BC SiR advantages.

molecules.[24–26] Studies indicate that borneol, when polymerized with cation, zwitterion, fluorine, and polysaccharides, demonstrates potent anti-adhesion properties against both bacteria and fungi.[27–30] Although this stereochemical strategy has been successfully applied to many types of surfaces or polymers, there are still few research reports on the modification of elastic SiR materials. Recently, studies on antimicrobial-functionalized silane coupling agents have provided valuable insights for synthesizing intrinsically antimicrobial SiR. By incorporating thiol-functionalized siloxanes with nitroso groups or introducing fluorinated siloxanes, these materials achieve candle soot crosslinking, effectively preventing biofilm formation. Therefore, functionalized siloxanes offer a promising method to endow substrates with antimicrobial properties.[31,32] Using (3-aminopropyl)-triethoxysilane (APTES) as a precursor, the synthesized phosphite-protonated siloxane exhibited excellent antimicrobial effects through the formation of a siloxane network, and the guanidine-functionalized siloxane-based antimicrobial agent demonstrated remarkable antibacterial activity.[33,34] Some research has shown that the addition of rigid structures can improve the mechanical properties of SiR.[35–37] Considering the preparation process of room-temperature cured SiR. Given that borneol is a rigid terpenoid compound with notable antimicrobial properties,[38] using borneol-based siloxanes as crosslinkers for SiR is promising.

Here, we aim to develop a type of bulk SiR with intrinsically antimicrobial properties (**Scheme 1**). To achieve the enrichment of stereochemical structures and enhance functionality, the bifunctional bornyl-siloxane crosslinker (BC) was synthesized through an aza-Michael addition reaction, utilizing two equivalents isobornyl acrylate (BA) as a precursor with one equivalent of APTES. Subsequently, by conducting a hydrolytic condensation reaction with hydroxy-terminated polydimethylsiloxane (PDMS), antimicrobial BC SiR can be prepared on a large scale at room temperature without the need for additional solvents, while exhibiting good elastic recovery performance (Scheme 1c). Based on optimized crosslinker ratios of BC, antimicrobial adhesion properties were achieved. Further, in vivo animal experiments were carried out in this work to confirm its good effectiveness in reducing infection risk as an implant.

2. Results and Discussion

2.1. Preparation and Characterization of BC and BC_x SiR

The structure of double substituted BC was characterized through ^{1}H NMR spectroscopy and Fourier Transform Infrared Spectroscopy (FTIR; **Figure 1a**; Figure S1a, Supporting Information). Figure 1a shows the ^{1}H NMR spectra of BC, using mono substituted bornyl-siloxane molecules as a control. The signals corresponding to n' (δ 2.71 ppm) and m' and b' (δ 2.35 ppm) of BC molecules emerged, with an integrated area ratio of 2/3 for their respective absorption peaks. In the spectrum of BC, signals were observed at chemical shifts of 2.80, 2.54, and 2.42 ppm, corresponding to the hydrogen proton at the 2, 1, and 3 positions of the monosubstituted molecules, with identical integral area ratios. These can be attributed to the presence of a small amount of mono substituted molecules in the product (≈12% mole rate, Formula 2). In addition, the absorption signal of hydrogen proton on $-NH_2$ of APTES molecules appeared at δ 1.43 ppm. For BA, the signals at chemical shifts of 5.80, 6.08, and 6.31 ppm corresponded to the characteristic absorption peaks

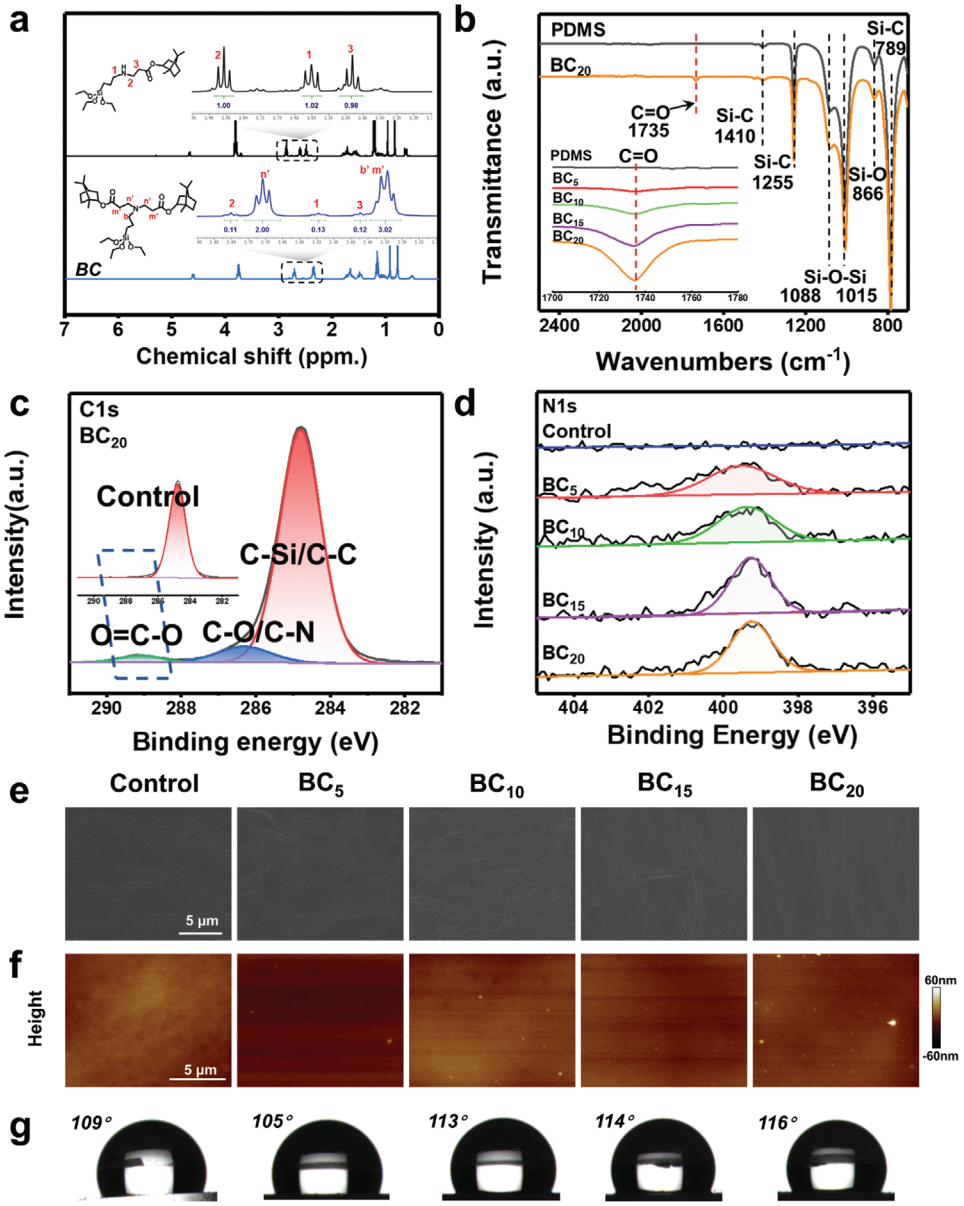

Figure 1. Preparation and Characterization of the BC_x SiR. a) ^1H NMR of mono borneol-substituted molecules and BC. b) FTIR spectra and c, d) XPS spectra of PDMS and the BC_x SiR. (c) C1s and (d) N1s high-resolution spectra of the above-mentioned samples. e) SEM and f) AFM height images of the samples' surfaces. g) WCA images of the above samples.

of the proton on the C═C double bond. The absorption peaks mentioned in APTES and BA disappeared in the BC spectrum. The appearance of these two new absorption peaks and the presence of the corresponding hydrogen proton attribution at each of the BC further proved the successful synthesis of the double substituted BC molecules (Figure S1a, Supporting Information).

FTIR was used to further analyze the changes in key chemical bonds. The FTIR results (Figure S1b, Supporting Information) revealed absorption peaks at 3364 and 1593 cm^{-1}, corresponding to the stretching and bending vibrations of the N–H group in APTES, respectively. Additionally, absorption peaks at 1735 and 1637 cm^{-1} were observed for BA molecules, corresponding to the stretching vibrations of C═O and C═C bonds, respectively. In the case of BC, no significant absorption peak of the N–H from APTES and the C═C absorption peak from BA was found, initially indicating the successful progress of the aza-Michael addition reaction.

Figure S2 (Supporting Information) illustrates the cured process of the BC_x SiR. At room temperature, the raw materials BC and PDMS were thoroughly mixed and poured into molds of specific sizes. The curing process was formed through the hydrolysis of BC_x and its crosslinked hydrolytic condensation with hydroxyl-terminated PDMS. The system was transitioned from a liquid state to a solid state, indicating the completion of SiR curing. BC SiR exhibited a white and opaque appearance

(Scheme 1b). Figure 1b depicts the FTIR spectra of the basic ingredients PDMS and BC_{20}. Compared to the blank PDMS, an additional absorption peak corresponding to the C═O bond was observed at 1735 cm^{-1} for the BC_{20} group. Regularly, for the BC_5, BC_{10}, BC_{15} and BC_{20} groups, absorption peaks at 1735 cm^{-1} gradually increase in the FTIR spectra (Figure 1b inset), which provided preliminary evidence of the successful synthesis of the BC_x SiR.

Further surface detailed elemental information analysis was conducted through X-ray Photoelectron Spectroscopy (XPS). As a commercially available SiR product, Sylgard 184 was used as control. Figure S3a (Supporting Information) shows XPS wide-scan spectra, absorption peaks corresponding to Si2p, C1s, O1s, and N1s were observed for the BC_x SiR. However, no N1s absorption peak was detected in the control group. Further analysis of the samples was conducted using high-resolution spectra. Compared with the control group, The C1s spectrum (Figure 1c; Figure S3, Supporting Information) from XPS of BC_x SiR reveals new absorption peaks at 288.8 eV for O═C—O bonds, and signals at 286.8 and 285.4 eV attributed to C—O bonds and C—N bonds in BC structure. Conversely, no significant absorption signals for the above signals were observed in the control group (Figure S3, Supporting Information). While from the high resolution N1s spectrum (Figure 1d), with the increase of BC content, the absorption peak of the N1s signal gradually increased and no absorption peak was observed in the control group, because of the N element only in BC molecules. Table S1 (Supporting Information) provides the proportions of surface elements in different BC_x SiR. As the amount of BC increased, the proportion of element C increased from 53.85% to 58.65% and the proportion of element O decreased from 22.61% to 21.24%. Hence, the C/O elements ratio increased gradually, from 2.38/1 to 2.76/1. Further, the proportion of BC units on the material surface was calculated. The theoretical elemental C/O ratios of the two types of units (BC for 7.25/1 and PDMS for 2/1) were used for these calculations. The results, as shown in Table S1 (Supporting Information), indicated that the surface molar fractions of BC units in BC_5, BC_{10}, BC_{15}, and BC_{20} are 7.33%, 9.33%, 12.02%, and 14.46%, respectively.

Surface morphology was tested using Scanning Electron Microscope (SEM, Figure 1e). All samples showed certain textures and wrinkles, compared to the control group, the BC_x SiR exhibited no significant differences. The slightly wrinkled morphology observed in the SEM images may result from high-energy electron beam interactions with the SiR surface, as in previous studies about SEM images for the SiR.[39,40] This effect is consistent across both the control group and the BC SiR samples, indicating a similar surface morphology. Compared to the SEM, Atomic Force Microscope (AFM) can achieve higher spatial resolution in assessing surface roughness and the true physical morphology of surface features.[41–43] Therefore, AFM testing was performed for a more in-depth examination.[44–47] The images are shown in Figure 1f. For the control group, the surface is smooth, with a corresponding root mean square roughness (Rq) of 5.83 nm. In comparison, the roughness of BC_5, BC_{10}, BC_{15}, and BC_{20}, as observed from the height map, was 15.30, 6.27, 4.17, and 5.59 nm, respectively. The surfaces were smooth, with no significant protrusions. Additionally, no obvious phase separation structure was observed (Figure S4, Supporting Information). These results from SEM and AFM confirmed the good uniformity of the BC_x SiR. These combined findings confirm the BC is evenly distributed in the BC SiR.

Furthermore, the WCA variation of the BC_x SiR was investigated. With an increase in BC content, WCA shows an upward trend, rising from 105° to 116° (Figure 1g). Combined with the results of AFM, all samples exhibit smooth surfaces, suggesting that the increase in WCA with higher BC content was not due to surface roughness. Instead, the increase is attributed to the specific hydrophobic carbon cage structure of BC. In summary, all samples exhibit hydrophobicity performance, and the structure modification maintains the hydrophobic characteristics of SiR.

2.2. Mechanical and Thermal Properties

The influence of different BC proportions on the mechanical properties of SiR was evaluated. **Figure 2**a shows the different SiR tensile samples. BC modification causes the BC_x SiR to appear opaque white. Figure 2b shows photographs of the tensile test process for BC_{20} and Sylgard 184. The images indicated that Sylgard 184 specimen break first, proved that its elongation at break was lower than BC_{20}. Figure 2c represents the stress–strain curves. BC_{20} exhibited the tensile strength and highest elongation at break among the BC_x SiR, measuring 426.9 kPa and 246.7%, respectively. The tensile strength was 290.6, 307.3, and 346.3 kPa, respectively (Figure 2d); and the elongation at break of BC_5, BC_{10}, and BC_{15} was 82.3%, 115.6%, and 171.3%, respectively (Figure 2e). It is worth noting that as the BC content increases, both the elongation at break and tensile strength results showed an increasing trend. On one hand, the introduction of borneol's rigid structure increases the content of rigid chain segments in the polymer, thereby enhancing its mechanical properties. On the other hand, the rigid polar structure of borneol promotes greater molecular chain entanglement of polysiloxane and crosslinking density.[36,37,48–50] Although the BC_{20} SiR exhibited significantly improved elongation at break compared to Sylgard 184 (169.7%), the tensile strength was lower than that of Sylgard 184 (969.6 kPa). As the BC content increases, the elastic modulus of the BC_x SiR showed a slight decreasing trend (Figure 2f). This decrease is likely due to agglomeration and self-crosslinking caused by the increased amount of BC.[49]

Thermogravimetric Analyzer (TGA) was further conducted to evaluate the thermal degradation characteristics of the BC_x SiR. Figure 2g, h, respectively represent the TGA and DTG curves of the BC_x SiR under an air atmosphere. The mass loss mainly occurred in two stages. The first thermal degradation process occurred from 270 to 400 °C. From BC_5 to BC_{20}, the corresponding mass losses were 5.85%, 8.14%, 10.30%, and 15.20%, respectively, which was attributed to the decomposition of the borneol cage of BC molecules. Because the energy of the C—N bond (305 kJ mol^{-1}) or C—O (345 kJ mol^{-1}) is lower than that of the Si—O bond (460 kJ mol^{-1}), as the temperature rises, the C—N bond or C—O bond breaks first, leading to the mass loss of the borneol structure.[35,51–53] Furthermore, a second thermal degradation step was observed between 400 and 600 °C, corresponding to the maximum mass loss, attributed to the degradation of the siloxane main chain.[52] From the DTG curve, it was observed that as the amount of BC units increased, the second peaks of the BC_x

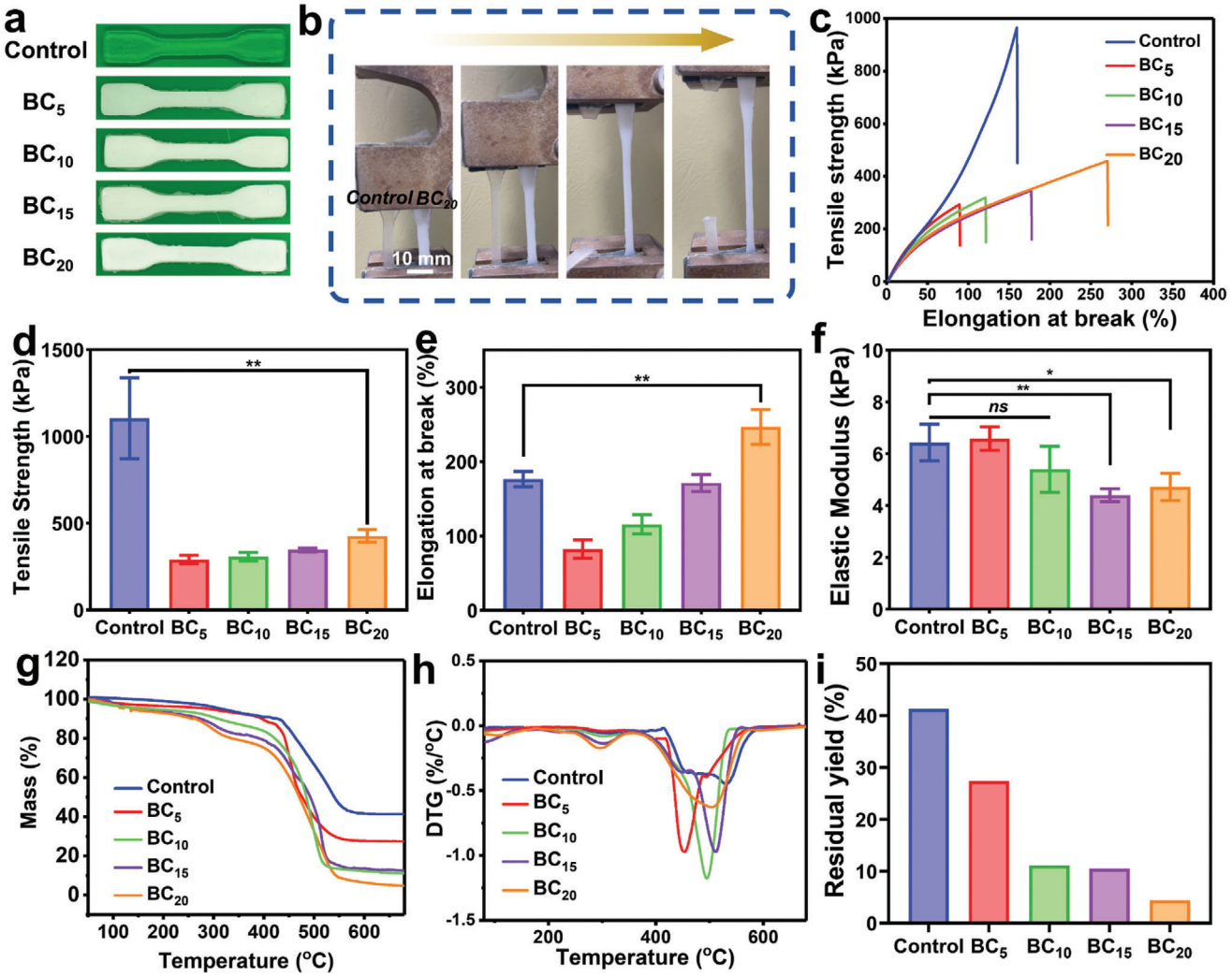

Figure 2. Mechanical and thermal properties of the SiR. a) Photographs of different tensile samples. b) Images of mechanical properties test of BC_{20} and control samples. c) Stress–strain curves, d) tensile strength, e) elongation at break and f) elastic modulus of the samples. g) TGA, h) DTG and i) residual yield of the SiR. $^{*}p < 0.05$, $^{**}p < 0.01$, ns $p > 0.05$.

SiR showed a trend toward higher temperatures. This change suggested that crosslinking of siloxanes can delay the degradation of SiR at high temperatures. On one hand, this trend may be due to the rigid cage structure of BC increasing the entanglement of the siloxane chains, limiting the mobility of the siloxane main chain and thus inhibiting the formation of siloxane oligomers. On the other hand, during thermal degradation, the decomposition of BC may form a carbonaceous layer, creating a physical barrier that delays further degradation of the siloxane.[35,52] As the temperature continues to rise, all samples reach a constant weight. Interestingly, the residual yield decreases with increasing BC content (Figure 2i). The residual yield for the control group was 41.32%, while for BC_5, BC_{10}, BC_{15}, and BC_{20}, the rates were 27.40%, 11.14%, 10.51%, and 4.44%, respectively. First, in the air environment, PDMS units eventually degrade into SiO_2 residues.[54] Therefore, as the BC content increases, the proportion of PDMS decreases, leading to a reduction in residue. Additionally, during thermal degradation, BC structures undergo oxidation, producing various free radicals and volatile organosilicon compounds, leading to a lower residual yield. These two factors contributed to the reduction in residual yield.[55]

2.3. Anti-Bacterial Adhesion Assay

The anti-adhesive effects of the above samples against *Escherichia coli* (*E. coli*) and *Staphylococcus aureus* (*S. aureus*) were evaluated using an anti-bacterial adhesion model.[56] **Figure 3a** presents the anti-bacterial adhesion results. Compared to the control group, the anti-bacterial adhesion effects gradually improved with the increase in BC addition. Figure 3b,c respectively show the bacterial adhesion quantities of the samples. For *E. coli*, the anti-adhesion rates of BC_5, BC_{10}, BC_{15}, and BC_{20} were 70.3%, 81.5%, 92.7%, and 99.4%, respectively; while for *S. aureus*, the anti-adhesion rates were 77.6%, 88.9%, 93.2%, and 97.3%, respectively. Combining the previous analysis results, as the BC content gradually

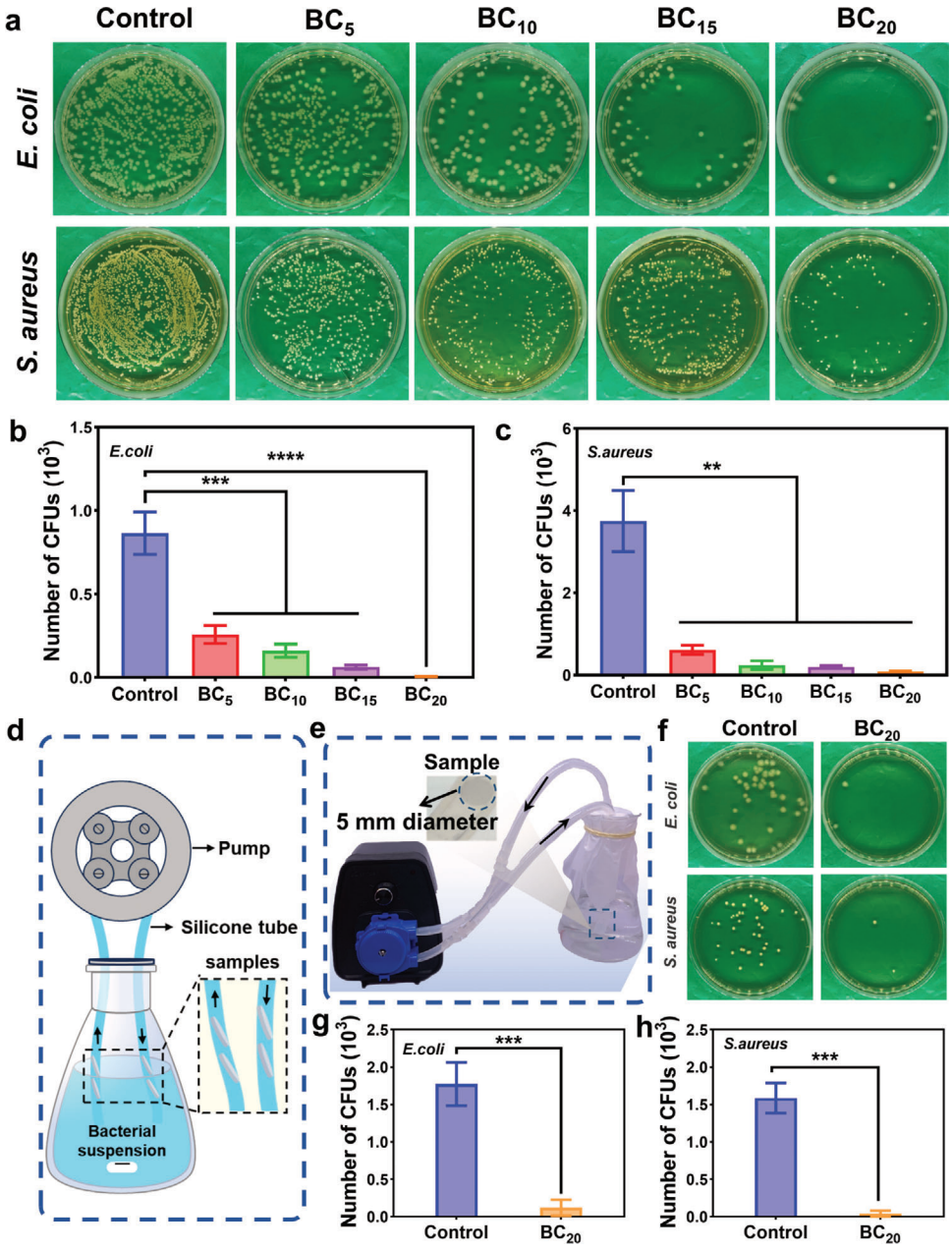

Figure 3. Anti-bacterial adhesion assay of the different SiR under co-culture and hydrodynamic conditions. a) The images of co-culture CFUs in plates. The number of CFUs calculated from b) *E. coli* and c) *S. aureus* groups. d) Schematic illustration and e) actual images of the hydrodynamic circulation devices. f) The CFUs number of the samples under hydrodynamic conditions and their statistical results of g) *E. coli* and h) *S. aureus*. $^{**}p < 0.01$, $^{***}p < 0.001$, $^{****}p < 0.0001$.

increased, the borneol structure present on the surface of the SiR material increased, leading to a gradual decrease in the amount of bacterial adhesion, both for Gram-negative and Gram-positive bacteria. As an antimicrobial material, the non-release property is crucial to prolong the antimicrobial effect and ensure biosafety. Therefore, to further verify whether SiR resisted bacterial adhesion by releasing molecules, an inhibition zone experiment was conducted. The results, as shown in Figure S5 (Supporting Information), did not produce significant ZOI. Thus, the BC_x SiR did not prevent bacterial adhesion by releasing molecules, but rather by its anti-adhesion effect on borneol molecules.

We know that SiR is one of the main materials used in clinical catheters. Therefore, to simulate the use of clinical catheters, the anti-bacterial adhesion assay under hydrodynamic conditions was carried out.[57] The BC_{20} SiR was used in this experiment. Figure 3d illustrates the schematic design for the hydrodynamic device. BC_{20} and control samples were cut into 5 mm diameter sizes, and then placed inside a catheter. Air bubbles were removed to ensure the bacterial suspension filled the catheter completely. The suspension was placed in a conical flask stirred and allowed to flow over the sample surface at 5 mL min^{-1} for 24 h, followed by colony counting to assess anti-bacterial adhesion

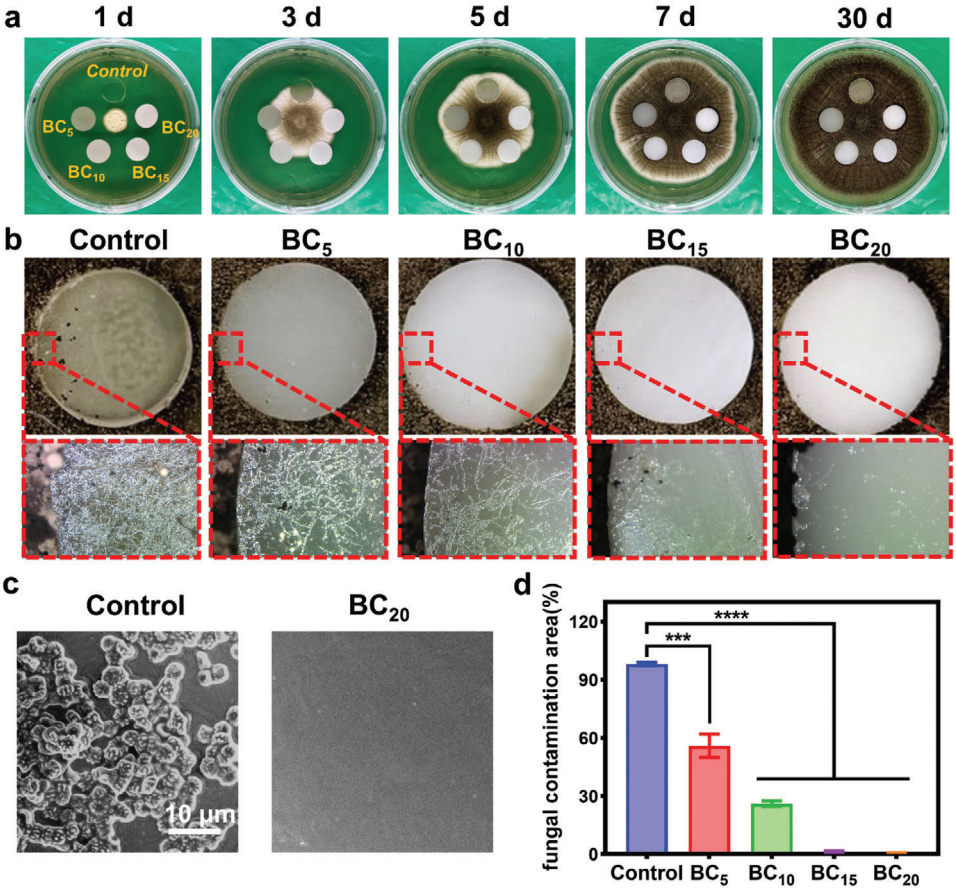

Figure 4. Anti-mold assay. a) Digital photos and b) microscopic images of the mold repelling effect of the samples in 30 d. c) SEM images of control and BC_{20} edge contaminated by *A. niger*. d) Contamination area of different samples edge by *A. niger*. $^{***}p < 0.001$, $^{****}p < 0.0001$.

performance. The actual circulation device shown in Figure 3e, f, shows the colony counting results, while Figure 3g, h, represents the statistical analysis of *E. coli* and *S. aureus*, respectively. The results showed that the bacterial adhesion on the BC_{20} SiR sample was significantly reduced compared to the control group. This experiment demonstrated that the BC_{20} SiR sample has good anti-bacterial adhesion performance in a hydrodynamic fluid environment, indicating a potential for application in clinical catheters.

2.4. Long-Lasting Anti-Mold Assay

Compared to the emphasis on anti-bacterial properties, anti-mold properties are often overlooked.[58] The ability of the BC_x SiR to anti-mold contamination was assessed using the filamentous fungus *Aspergillus niger* (*A. niger*). The "mold landing model" was used to evaluate the long-lasting mold repelling properties of BC_x SiR. **Figure** 4a shows the growth status of *A. niger* on days 1, 3, 5, 7, and 30. From the status on the 30th day, it could be observed that the surface of the control was contaminated by *A. niger*, while the BC_x SiR edges were clear. To further verify its repelling effect, microscopic observation of the material surface was conducted (Figure 4b), providing surface images and magnified images of the edge. From the surface images, it could be observed that the surface of the control group was contaminated by mold, with black spore clusters present, while the BC_x SiR showed no obvious contamination by black spore clusters. From the magnified edge images, it was clear that the edge of the control group was covered with hyphae, indicating relatively severe contamination. In contrast, for the BC_x SiR, with the increase of BC content, the hyphae on the sample edge were significantly reduced, demonstrating the excellent mold repelling effect. Research has shown that molds first produce hyphae during their growth process, and as the hyphae mature, spores are generated.[59] When *A. niger* grows on solid culture media and comes into contact with the sample, surfaces with anti-mold adhesion properties can prevent contamination by hyphae. In contrast, surfaces without anti-mold adhesion properties are more likely to be contaminated by hyphae, leading to spore accumulation on the sample surface. SEM further observed the contamination of the BC_{20} and control groups' surfaces (Figure 4c). There are many spores on the surface of the control group, indicating vigorous mold growth and spore colonization. In contrast, no obvious contamination can be observed on the BC_{20} SiR surface, further verification of the anti-mold effect of BC_{20}. Figure 4d presents the statistical analysis of surface edge contamination of all samples by using ImageJ software. For the control group, the contaminated surface revealed a coverage area of 99.8%. With the gradual

increase of BC content from BC_5 to BC_{20}, the coverage areas were 55.9%, 26%, 1.1% and 0.7%, respectively. This mold repelling effect was observed continuously for 30 days. Therefore, the BC_{20} SiR can also act as a good and long-lasting mold repelling material.

2.5. In Vivo Antimicrobial Performance Evaluation

In order to further evaluate the in vivo anti-bacterial performance of the BC_{20} SiR, a mice subcutaneous implant model of bacterial infection was designed (**Figure 5**a).[60,61] In brief, the sterilized samples were first immersed in a bacterial solution to simulate bacterial contamination of the implanted device. Then the samples were implanted into the mice's back, designated as day 0. The mice were monitored at different time points to determine the infection status on the following days. Bacteria counts and H&E staining were conducted on days 1, 3, and 5. Figure 5b shows photographs of back infections in mice at different time points. In the control group, there were evident abscesses around the sample, indicating severe bacterial infection after implantation. Moreover, on the 5th day, suppuration still existed. However, in the BC_{20} group, no significant abscess formation was observed, and the surrounding tissue structure remained clear. To further determine the infection status of mice, bacteria counting experiments were performed. Figure 5c shows the results of bacterial cultures not only from the surface of the control group but also from ground tissue surrounding the implant. From the bacteria counting results on day 1 to day 5, it could be seen that the bacteria count in the control group was significantly higher than that in the BC_{20} group. For the control group, the colony count results showed that severe bacterial infection occurred on the first day of subcutaneous implantation in mice. Despite a decreasing trend in bacterial counts observed in the surrounding tissues, likely due to the host immune response and pus formation,[62,63] by the 5th day, the number of bacteria in the surrounding tissues could completely cover the surface of the solid culture medium. For the BC_{20} group, on day 5, only a small number of bacteria existed in the surrounding tissues and few bacteria could be detected on the materials surface. Figure 5d, e, provides a statistical analysis of the numbers of CFUs in different days of tissue and materials. Significant differences were observed in bacteria CFUs on both the surrounding tissues and the material surfaces. These bacteria count results indicated that the BC_{20} SiR implants exhibited excellent resistance to bacterial infections. This was mainly attributed to the fact that during the surgical implantation process, the surface borneol molecules effectively prevented bacterial adhesion, thereby reducing the risk of infection.

H&E staining of tissue sections surrounding the material further confirmed this capability. On days 1, 3, and 5, the control group showed significant aggregation of inflammatory cells, indicating infection in the mice. In contrast, for the BC_{20} SiR, a slight accumulation of inflammatory cells was observed on day 1, diminished by day 3, and no obvious inflammatory cells were found by day 5 (Figure 5f). This could be due to the mice's immune system gradually clearing the small number of bacteria, thereby reducing the occurrence of inflammation. These in vivo results suggested that BC_{20} SiR, as an implantable material, has the potential to reduce the risk of infection associated with medical implants.

2.6. In Vitro and in Vivo Biosafety Assessment

Biocompatibility or cellular/tissue toxicity are key concerns for the feasibility of biomedical materials. Cell cytotoxicity testing was conducted first by using the standard thiazolyl blue tetrazolium bromide (MTT) method.[27] Fluorescence Imaging was used to observe the cell structure. Mouse fibroblast cells (L929) cells exhibited a normal spindle-shaped morphology with intact cytoskeletal structure (**Figure 6**a). Meanwhile, the MTT results showed that in the cell, BC_{20} and control groups, all groups exhibited good cell viabilities of 99.9%, 97.9%, and 99.8%, respectively (Figure 6b). Furthermore, the blood compatibility was investigated. DIW and NS groups were chosen as positive and negative controls, respectively. As shown in Figure 6c,d, no hemolysis was observed with the BC_{20} SiR, and the hemolysis rate was less than 5%.

In addition, a subcutaneous implantation model in mice was employed to evaluate the in vivo biocompatibility of the BC_{20} SiR. As shown in Figure 6e, compared to the control group, the H&E staining results of the surrounding tissues of BC_{20} were all normal skin tissues, without obvious signs of inflammation, thus indicating its good in vivo biocompatibility.

3. Conclusion

In summary, with the help of the aza-Michael addition reaction, we prepared a double substituted bornyl-siloxane crosslinker, BC molecule, which provides a molecular basis for solvent-free synthesis of anti-microbial SiR under room temperature. As BC molecules served as novel stereochemical modifiers, the resulting BC SiR inherently possessed anti-bacterial and anti-mold adhesion properties without requiring further modification. The BC_{20} SiR cross-linked network exhibited excellent anti-bacterial and anti-mold adhesion, as well as good mechanical properties. The in vitro dynamic fluid co-culture models and in vivo anti-bacterial experiments have both demonstrated its remarkable potential for use as a SiR material in medical implants. Since the cross-linking points of the BC_x SiR were only generated by BC molecules, the tensile strength and elastic modulus need to be further improved, which is a key issue to be addressed in subsequent work. Besides, to optimize this approach, a precise and controlled chemical reaction process is essential for achieving efficient, continuous industrial-scale production. Moreover, due to the siloxane structure, BC can undergo hydrolysis for covalent surface modification on most hydrophilic surfaces, which is also promising in the field of antimicrobial coatings.

4. Experimental Section

Experimental Materials: (3-aminopropyl)-triethoxysilane (APTES, 99%) was purchased from Dongguan Shanyi Plastics Co., Ltd. Isobornyl acrylate (BA, 99%) was obtained from RYOJI Chemical Co., Ltd. Hydroxy-terminated polydimethylsiloxane (PDMS, 98%) was acquired from Shandong Dayi Chemical Co., Ltd. Dibutyltin dilaurate (DBTDL, 95%)

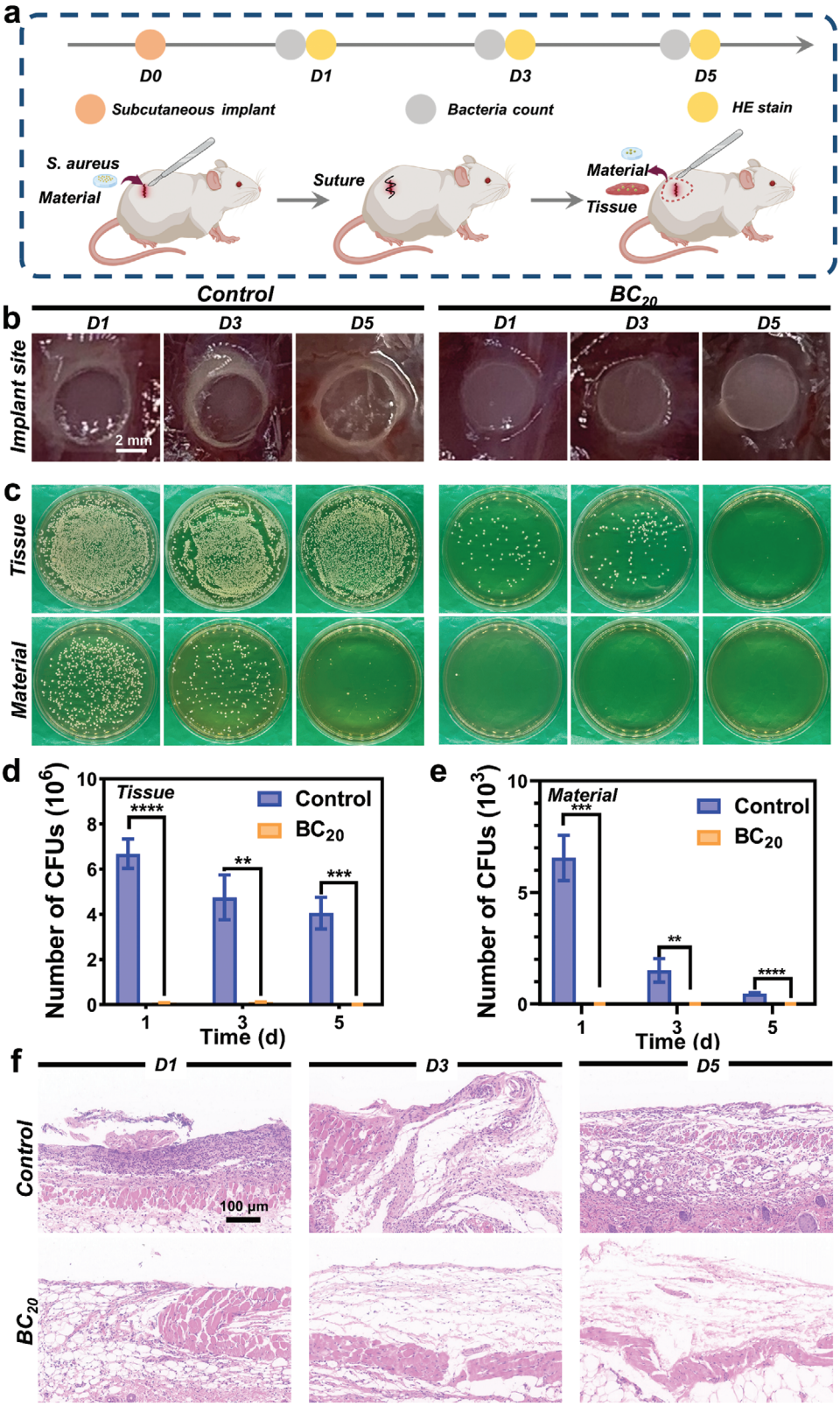

Figure 5. In vivo antimicrobial performance. a) Scheme of the in vivo implantation experiment. b) Photographs of the materials on the mice back at different time points. c) Photographs of the bacterial count of its surrounding tissue and materials and d, e) its statistical analysis. f) H&E staining of surrounding tissue. $^{**}p < 0.01$, $^{***}p < 0.001$, $^{****}p < 0.0001$.

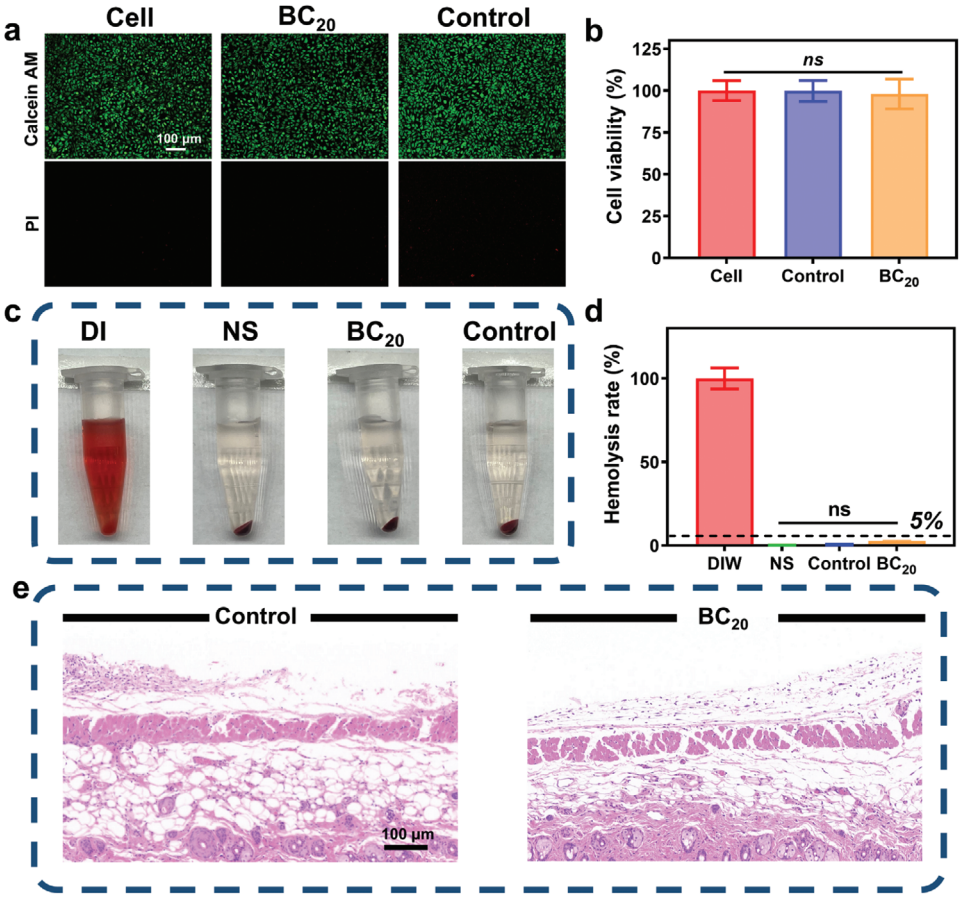

Figure 6. In vitro and in vivo biosafety assessment of SiR. a) Fluorescence microscopy images of L929 cells after 24 h incubation with SiR. b) Cell viability evaluation of different samples by MTT method. c) Hemolysis assays results and d) hemolysis rate. e) H&E stain of the surrounding tissues. ns $p > 0.05$.

was procured from Alfa Aesar (China) Chemical Co., Ltd. The Sylgard 184 was sourced from Songsen New Materials Technology Co., Ltd (Shenzhen). Ethanol (99.7%) was bought from the Damao Chemical Plant (Tianjin). RPMI 1640 medium (RPMI 1640), penicillin-streptomycin and Fetal Bovine Serum trypsin were obtained from Gibco Life Technologies (Beijing, China). Calcein-AM/PI Double Stain Kit and thiazolyl blue tetrazolium bromide (MTT) were obtained from Solarbio Science & Technology Co., Ltd. (China). Sodium dodecyl sulfate (SDS, 98%) was obtained from Aladdin Ltd. (Shanghai, China). Tryptone soy agar (TSA) and trypticase soy broth (TSB) were obtained from Sinopharm Chemical Reagent (China). *E. coli* (ATCC25922), *S. aureus* (ATCC25923), and *A. niger* (CICC41254) were obtained from the China General Microbiological Culture Collection Center. Mouse fibroblast cells (L929) were sourced from the Cell Resource Center of the Chinese Academy of Medical Sciences/Peking Union Medical College, Beijing, China. Red blood cells were taken from the hearts of SD rats and mixed with sodium citrate to obtain fresh citrated whole blood (CWB). Female BALB/c mice (5 weeks old, 14–18 g) were purchased from Beijing Vital River Laboratory Animal Technology Co., Ltd.

Preparation of BC and its Crosslinked SiR: BC was prepared by the aza-Michael addition reaction.[64] The amine group of APTES enables the Michael addition with two molecules of the acrylate compounds.[65] To maximize the antibacterial effect of the stereochemically functional molecules, dual stereochemical functionalization of the cross-linker was prepared. APTES and BA were added to a reaction flask at a molar ratio of 1:2, followed by the addition of an equivalent volume of anhydrous ethanol. The mixture was stirred and reacted at 65 °C for 1 day. For comparison, monosubstituted compounds were synthesized under the same conditions using APTES and BA in a molar ratio of 1:1. After rotary evaporation, vacuum drying and dialysis purification, double substituted BC was obtained with a purity of 89.2% and a yield of 91.6% respectively (Figure 1a, Formula 1). The relevant calculation formula is as follows:

$$\text{BC mole fraction } (\%) = \frac{\frac{I_{di}}{n_{H-di}}}{\frac{I_{di}}{n_{H-di}} + \frac{I_{mono}}{n_{H-mono}}} \times 100\% \quad (1)$$

$$\text{mono} - \text{molecules mole ratio } (\%) = \frac{\frac{I_{mono}}{n_{H-mono}}}{\frac{I_{di}}{n_{H-di}}} \times 100\% \quad (2)$$

Here, I_{mono} and I_{di} represent the integral areas of the characteristic peaks corresponding to the mono-molecules and di-molecules respectively. The $n_{H\text{-}mono}$ and $n_{H\text{-}di}$ represent the number of protons in the structural formula.

BC was blended with PDMS in various weight percentages (5%, 10%, 15%, and 20%) in a reaction flask, and the mixture was vigorously stirred with a paddle stirrer for 15 min. Dibutyltin dilaurate (DBTDL) was then added, and stirring was continued rapidly for another 15 min. Afterward, the mixture was placed in a vacuum oven to degas and remove air bubbles. Finally, the degassed mixture was poured into moulds and cured at room temperature. After five days, the curing process was completed to obtain BC cured SiR in different ratios (BC_5, BC_{10}, BC_{15} and BC_{20}, Scheme 1).

Characterization: FTIR spectrometer (Thermo Scientific Nicolet iS5, USA) was used to analyze the chemical structure of BC and the surface functional groups of the BC_x SiR. The ^1H NMR spectra were characterized using a Bruker 400 MHz spectrometer in $CDCl_3$ at room temperature. Surface elemental and compositional analyses of BC_x SiR were performed using XPS (Thermo Scientific K-Alpha, USA). The wettabilities of BC_x SiR were evaluated by measuring the static water contact angle (WCA) using JC2000C (Zhongchen Digital Technic Apparatus Co. Ltd., China). The thermodynamic properties of the samples were investigated using an HTG-1 TGA with a heating rate of 10 °C min^{-1} in air condition (Beijing Hengjiu Scientific Instrument Factory). Mechanical properties of different samples were evaluated using a Universal Testing Machine (MTS, E44.104, USA) at room temperature. The tensile testing was conducted at a strain rate of 50 mm min^{-1}. Dumbbell-shaped specimens with a thickness of 1 mm and a length of 50 mm were used for the tests. The surface morphology of the materials was examined under a 7 kV voltage using a MAIA3-TESCAN SEM (TESCAN, China). Further observation of the material surface morphology was conducted using an AFM (AFM-DMFASTSCAN2-SYS, Bruker, Germany). Cell morphology was observed using a Confocal laser scanning microscopy (CLSM, Leica SP5, Germany).

Anti-Bacterial Adhesion Assay: The anti-bacterial adhesion effects on SiR were quantitatively measured using a reported method.[66] Briefly, different SiR materials were cut into 8 mm diameter discs and sterilized by irradiating both sides with UV light for 15 min. The discs were then completely submerged in a bacterial suspension with a concentration of 10^7 colony-forming units mL^{-1} (CFUs mL^{-1}) and co-cultured for over 6 h.[56,67] Afterward, the discs were removed and gently rinsed three times with sterile saline on both sides to remove any non-adherent bacteria. The washed SiR was then submerged in 1 mL of sterile saline and ultrasonic treatment for 10 min to disperse the bacteria adhered to the surface into the saline. Subsequently, 100 µL of the resulting bacterial suspension was evenly spread on TSA agar and incubated at 37 °C for 24 h to count the CFUs. The anti-bacterial adhesion rate was calculated according to the following formula:

$$\text{Anti} - \text{bacterial adhesion ratio} \quad (\%) = \frac{A - B}{A} \times 100\% \tag{3}$$

where A and B are the CFUs numbers of the control group and experimental group, respectively.

Zone of Inhibition (ZOI): To investigate whether the BC_x SiR kills bacteria by releasing small molecules, a zone of inhibition assay was conducted.[68] Briefly, 100 µL of a bacterial suspension at a concentration of 10^7 CFU mL^{-1} was spread onto TSA plates. The samples were then placed on the surface of the TSA, and after 24 h of incubation, photographs were taken to observe any ZOI.

Long-Lasting Anti-Mold Assay: The anti-mold effects on the BC_x SiR were assessed using a reported method.[69,70] Briefly, the BC_x SiR was cut into 10.0 mm diameter circular samples and sterilized by irradiating both sides under UV light for 15 min. The samples were then placed flat on malt extract agar, 1–2 cm from the center of the Petri dish. Next, 10 µL of mold solution, mold spore suspension containing (1–5) × 10^8 spores mL^{-1}, was added to the center of the dish. The cultures were incubated at a constant temperature of 30 °C and relative humidity of 85% ± 5% for 30 days. The contamination of the BC_x SiR surfaces was observed and photographed. Commercially available Sylgard 184 SiR served as a control. The contamination by *A. niger* at the edges of the materials was observed by using SEM.

Anti-Bacterial Adhesion Assay under Hydrodynamic Conditions: SiR a primary component of catheter materials used clinically. To measure its anti-bacterial adhesion effects under hydrodynamic conditions, the BC_x SiR was placed inside a catheter for an in vitro circulation experiment.[57] The bacterial concentration was maintained at 10^8 CFUs mL^{-1} in sterile saline solution, with continuous co-culture for 24 h at a flow rate of 5 mL min^{-1}. Afterward, the BC_x SiR was removed and gently washed 3 times with sterile saline on both sides. The sample was then sonicated in 1 mL of sterile saline for 10 min. Next, 100 µL solution was spread onto the surface of TSA and incubated at 37 °C for 24 h for colony counting.

In vitro Biological Safety Assessment: Cell compatibility testing was performed using the MTT assay.[71,72] Prior to the experiments, the BC_x SiR was soaked in 75% ethanol.

MTT assay for cytotoxicity testing: the BC_x SiR materials (with a surface area of ≈3 cm^2) were submerged in 1 mL of RPMI 1640 medium and incubated for 24 h at 37 °C, 95% air, and 5% CO_2 in a humidified incubator to obtain extracts from different materials. L929 cells were cultured in RPMI 1640 medium supplemented with 10% FBS, 100 µg mL^{-1} penicillin, and 100 µg mL^{-1} streptomycin at 37 °C, 95% air, and 5% CO_2 in a humidified incubator until reaching the logarithmic growth phase, then resuspended in fresh medium to form cell suspension. The cell suspension of L929 cells was seeded in a 96-well plate at a density of 8000 cells per well, with 100 µL per well. The plate was incubated for 24 h at 37 °C, 95% air, and 5% CO_2 in a humidified incubator. The medium was discarded from the wells, and 100 µL of the extract from different materials was added to each well, followed by incubation for 24 h. Each well received 10 µL of MTT solution (5 mg mL^{-1}) and was incubated for 4 h at 37 °C. Subsequently, 100 µL of SDS solution was added to each well, and the plate was gently shaken to ensure uniform dissolution. The plate was then placed in a microplate reader to measure absorbance at 570 nm, and relative cell viability was calculated using the following formula:

$$\text{Cell viability} \quad (\%) = \frac{Abs_{sample} - Abs_{blank}}{Abs_{cell} - Abs_{blank}} \times 100\% \tag{4}$$

Here, Abs_{sample} represents the absorbance of cells cultured with extracts from different SiR materials, Abs_{blank} represents the absorbance of the blank medium, and Abs_{cell} represents the absorbance of cells not treated with any samples.

Fluorescence Imaging: Cell viability was evaluated using live/dead cell staining after treatment with the BC_x SiR. Briefly, cell density was adjusted to 5 00 000 cells mL^{-1} and incubated for 24 h. After this incubation, the sample extract was added, and the cells were cultured for an additional 24 h. Subsequently, cells were stained with AM/PI under dark conditions for 30 min. The excess stain was then removed by washing the cells three times with sterile saline. Fluorescence images were captured using a CLSM.

Hemocompatibility Testing: Hemocompatibility testing was assessed using a reference method.[73,74] Briefly, 1 mL of anticoagulated rat whole blood was taken and mixed with 2 mL of saline. The mixture was centrifuged at 1500 rpm for 10 min, and the supernatant was discarded. Saline was added back to make up 3 mL, and the centrifugation was repeated, continuing this process 5 times until the supernatant became clear. The final supernatant was discarded, and 10 mL of normal saline was added to obtain a red blood cell suspension (RBCs). The RBCs were diluted fivefold with saline, and the BC_x SiR was then submerged in 1 mL of the diluted cell suspension and incubated at 37 °C on a shaker at 30 rpm for 3 h. Deionized water (DIW) and normal saline (NS) diluted RBCs were used as positive and negative controls, respectively. After incubation, the mixture was centrifuged at 2000 rpm for 10 min, and 100 µL of the upper layer was transferred to a 96-well plate. Absorbance at 545 nm was measured using a spectrophotometer. The calculation of the hemolysis rate is as follows:

$$\text{Hemolysis ratio} \quad (\%) = \frac{A_{sample} - A_{negative}}{A_{positive} - A_{negative}} \times 100\% \tag{5}$$

Here, A_{sample} represents the absorbance of the upper layer absorbance of different SiR samples, $A_{negative}$ represents the absorbance of the NS group, and $A_{positive}$ represents the absorbance of the DIW group.

In vivo Antimicrobial Performance: In vivo, anti-bacterial evaluation was used in mice subcutaneous implantation model.[75] The BC_x SiR samples were submerged in a sterile saline suspension of *S. aureus* (1 × 10^8 CFUs mL^{-1}) and incubated at 37 °C for 3 h. Subsequently, the samples were implanted subcutaneously into the dorsal region of mice. The mice were euthanized by cervical dislocation on days 1, 3 and 5, respectively. The surrounding tissues were surgically excised, homogenized using a tissue grinder, diluted in sterile saline, and 100 µL was plated for bacteria colony

counting. At the same time, the sample was taken out, and placed in sterile saline for ultrasound, and the bacteria colony count was performed. The surrounding tissues were also sectioned and evaluated histologically with hematoxylin and eosin (H&E) staining.

In vivo Biosafety Assessment: The in vivo biosafety was evaluated using a subcutaneous implantation model.[60,76] The samples were implanted into the dorsal area of mice, respectively. After 5 days, the mice were euthanized by cervical dislocation. The tissues surrounding the implanted SiR were observed histologically using H&E staining.

The animals were treated in accordance with the National Research Council's Guide for the Care and Use of Laboratory Animals and overseen by the SPF Animal Department at the China-Japan Friendship Hospital's Clinical Institute (Approval No. Zryhyy 12-20-08-3).

Statistical Analysis: In this experiments, *t*-test was used to evaluate the statistical significance of differences between groups. The results were reported as mean ± standard deviation (SD). ns $p > 0.05$, $^{*}p < 0.05$, $^{**}p < 0.01$, $^{***}p < 0.001$, $^{****}p < 0.0001$.

Supporting Information

Supporting Information is available from the Wiley Online Library or from the author.

Acknowledgements

This work was supported by the National Natural Science Foundation of China (52273118, 22275013), the Fundamental Research Funds for the Central Universities (QNTD2023-01), and the Joint Project of BRC-BC (Biomedical Translational Engineering Research Center of BUCT-CJFH) (XK2023-16, 2023-NHLHCRF-YXHZ-MS-02).

Conflict of Interest

The authors declare no conflict of interest.

Data Availability Statement

The data that support the findings of this study are available from the corresponding author upon reasonable request.

Keywords

antimicrobial, bornyl-siloxane, silicone rubber

Received: November 26, 2024
Revised: December 16, 2024
Published online:

[1] C. R. Arciola, D. Campoccia, L. Montanaro, *Nat. Rev. Microbiol.* **2018**, *16*, 397.
[2] B. Li, T. J. Webster, *J. Orthopaedic Res.* **2018**, *36*, 22.
[3] P. S. Stewart, T. Bjarnsholt, *Clin. Microbiol. Infect.* **2020**, *26*, 1034.
[4] S. Amin Yavari, S. M. Castenmiller, J. A. G. van Strijp, M. Croes, *Adv. Mater.* **2020**, *32*, 2002962.
[5] D. P. Calfee, *Annu. Rev. Med.* **2012**, *63*, 359.
[6] D. Davies, *Nat. Rev. Drug. Discov.* **2003**, *2*, 114.
[7] V. Sardar, N. Rajhans, A. Pathak, T. Prabhu, 14th International Conference on Humanizing Work and Work Environment HWWE-2016, Punjab, India **2016**.
[8] Q. Li, Y. He, J. Yan, Y. Li, J. Feng, Z. Wang, *Biomater. Sci.* **2023**, *11*, 7311.
[9] I. Fundeanu, H. C. Van Der Mei, A. J. Schouten, H. J. Busscher, *Colloids Surf., B* **2008**, *64*, 297.
[10] M. Bizjak, C. Selmi, S. Praprotnik, O. Bruck, C. Perricone, M. Ehrenfeld, Y. Shoenfeld, *J. Autoimmunity* **2015**, *65*, 64.
[11] Y. Zou, C. Liu, H. Zhang, Y. Wu, Y. Lin, J. Cheng, K. Lu, L. Li, Y. Zhang, H. Chen, Q. Yu, *Acta Biomater.* **2022**, *151*, 254.
[12] D. Bezuidenhout, D. F. Williams, P. Zilla, *Biomaterials* **2015**, *36*, 6.
[13] M. Lam, V. Migonney, C. Falentin-Daudre, *Acta Biomater.* **2021**, *121*, 68.
[14] J. Saunier, A. Khzam, N. Yagoubi, *J. Mech. Behav. Biomed. Mater.* **2022**, *136*, 105477.
[15] X. He, K. Gopinath, G. Sathishkumar, L. Guo, K. Zhang, Z. Lu, C. Li, E.-T. Kang, L. Xu, *ACS Appl. Mater. Interfaces* **2021**, *13*, 20708.
[16] G. Schmidmaier, M. Lucke, B. Wildemann, N. P. Haas, M. Raschke, *Injury* **2006**, *37*, S105.
[17] W. Peng, H. Yin, P. Liu, J. Peng, J. Sun, X. Zhang, Y. Gu, X. Dong, Z. Ma, J. Shen, P. Liu, *Chem. Eng. J.* **2021**, *412*, 128707.
[18] W. Peng, B. Fan, Y. Li, Y. Dong, W. Qian, X. Ji, D. Gan, P. Liu, J. Shen, *J. Mater. Chem. B* **2022**, *10*, 8013.
[19] K. Ding, Y. Wang, S. Liu, S. Wang, J. Mi, *RSC Adv.* **2021**, *11*, 39950.
[20] A. Mondal, P. Singha, M. Douglass, L. Estes, M. Garren, L. Griffin, A. Kumar, H. Handa, *ACS Appl. Mater. Interfaces* **2021**, *13*, 43892.
[21] S. Li, Z. Guo, H. Zhang, X. Li, W. Li, P. Liu, Y. Ren, X. Li, *ACS Appl. Bio Mater.* **2021**, *4*, 3166.
[22] K. Benedict, B. R. Jackson, T. Chiller, K. D. Beer, *Clin. Infect. Dis.* **2019**, *68*, 1791.
[23] C. Farges, O. Cointault, M. Murris, L. Lavayssiere, S. Lakhdar-Ghazal, A. Del Bello, A.-L. Hebral, L. Esposito, M.-B. Nogier, F. Sallusto, X. Iriart, E. Charpentier, J. Guitard, F. Muscari, C. Dambrin, L. Porte, N. Kamar, S. Cassaing, S. Faguer, *Transplant Infectious Disease* **2020**, *22*, e13200.
[24] Z. Xie, G. Li, X. Wang, *Racing for the Surface*, (Eds: B. Li, T.F. Moriarty, T. Webster, M. Xing), Springer International Publishing, Cham **2020**, pp. 431–456.
[25] C. Pang, B. Li, Z. Tu, J. Ling, Y. Tan, S. Chen, L. Hong, *ACS Appl. Mater. Interfaces* **2024**, *16*, 38429.
[26] M. Burenjargal, T. Narangerel, T. Batmunkh, A. Dong, S. Idesh, *Food Science & Nutrition* **2023**, *11*, 5736.
[27] P. Zhang, X. Chen, F. Bu, C. Chen, L. Huang, Z. Xie, G. Li, X. Wang, *ACS Appl. Mater. Interfaces* **2023**, *15*, 9926.
[28] Q. Cheng, A. B. Asha, Y. Liu, Y.-Y. Peng, D. Diaz-Dussan, Z. Shi, Z. Cui, R. Narain, *ACS Appl. Mater. Interfaces* **2021**, *13*, 9006.
[29] F. Song, L. Zhang, R. Chen, Q. Liu, J. Liu, J. Yu, P. Liu, J. Duan, J. Wang, *ACS Appl. Mater. Interfaces* **2021**, *13*, 33417.
[30] Q. Cheng, Y.-Y. Peng, A. B. Asha, L. Zhang, J. Li, Z. Shi, Z. Cui, R. Narain, *Biomater. Sci.* **2022**, *10*, 1787.
[31] H. Xu, D. Jia, S. Guo, X. Zheng, W. Yang, H. Chen, Y. Zhang, Q. Yu, *J. Colloid Interface Sci.* **2025**, *679*, 191.
[32] Y. Lin, H. Zhang, Y. Zou, K. Lu, L. Li, Y. Wu, J. Cheng, Y. Zhang, H. Chen, Q. Yu, *J. Mater. Sci. Technol.* **2023**, *132*, 18.
[33] L. Zhang, G.-Q. Zheng, X.-L. Chen, S.-Q. Guo, F.-R. Zeng, B.-W. Liu, X.-L. Zeng, X.-S. Lan, Y.-Z. Wang, H.-B. Zhao, *ACS Materials Lett.* **2023**, *5*, 2398.
[34] F. V. Drozdov, A. N. Tarasenkov, M. S. Parshina, G. V. Cherkaev, E. N. Strukova, A. M. Muzafarov, *J. Organomet. Chem.* **2020**, *918*, 121243.
[35] X. Yang, Q. Li, Z. Li, X. Xu, H. Liu, S. Shang, Z. Song, *ACS Sustainable Chem. Eng.* **2019**, *7*, 4964.
[36] Q. Li, X. Huang, H. Liu, S. Shang, Z. Song, J. Song, *ACS Sustainable Chem. Eng.* **2017**, *5*, 10002.
[37] L. Guo, X. Yang, F. Dong, Y. Qian, J. Guo, X. Lin, H. Shaghaleh, W. Liu, X. Xu, S. Wang, S. Liu, *Mater. Chem. Phys.* **2020**, *247*, 122868.

[38] E. Christoforides, D. Mentzafos, K. Bethanis, *J. Incl. Phenom. Macrocycl. Chem.* **2015**, *81*, 193.
[39] H. T. Kim, O. C. Jeong, *Microelectron. Eng.* **2011**, *88*, 2281.
[40] K. Ning, Z. Tang, P. Xie, J. Hu, Z. Fu, *IEEE Transactions on Dielectrics and Electrical Insulation* **2023**, *30*, 31.
[41] J. Joshi, S. V. Homburg, A. Ehrmann, *Polymers* **2022**, *14*, 1267.
[42] G. Poletti, F. Orsini, C. Lenardi, E. Barborini, *J. Microsc.* **2003**, *211*, 249.
[43] Y. Li, J. Yang, Z. Pan, W. Tong, *Fuel* **2020**, *260*, 116352.
[44] L. Crouzier, A. Delvallée, S. Ducourtieux, L. Devoille, G. Noircler, C. Ulysse, O. Taché, E. Barruet, C. Tromas, N. Feltin, *Beilstein J. Nanotechnol.* **2019**, *10*, 1523.
[45] H. Huang, I. Dobryden, P.-A. Thorén, L. Ejenstam, J. Pan, M. L. Fielden, D. B. Haviland, P. M. Claesson, *Compos. Sci. Technol.* **2017**, *150*, 111.
[46] I. Keranov, T. G. Vladkova, M. Minchev, A. Kostadinova, G. Altankov, P. Dineff, *J. Appl. Polym. Sci.* **2009**, *111*, 2637.
[47] R. Jellali, J.-L. Duval, E. Leclerc, *Mater. Sci. Eng., C* **2016**, *65*, 295.
[48] Y. Qian, F. Dong, L. Guo, J. Guo, H. Shaghaleh, Y. Wang, X. Xu, S. Wang, S. Liu, *Polym. Degrad. Stab.* **2020**, *173*, 109068.
[49] M. Zuo, Z. Jiang, L. Guo, F. Dong, J. Guo, X. Xu, *ACS Omega* **2019**, *4*, 11921.
[50] W. Chen, Y. Liu, C. Xu, Y. Liu, Q. Wang, *RSC Adv.* **2017**, *7*, 39786.
[51] L. Jiao, H. Xiao, Q. Wang, J. Sun, *Polym. Degrad. Stab.* **2013**, *98*, 2687.
[52] Y. Wang, Y. Cai, H. Zhang, J. Zhou, S. Zhou, Y. Chen, M. Liang, H. Zou, *Polymer* **2021**, *236*, 124299.
[53] N. M. Florea, A. Lungu, P. Badica, L. Craciun, M. Enculescu, D. G. Ghita, C. Ionescu, R. G. Zgirian, H. Iovu, *Composites, Part B* **2015**, *75*, 226.
[54] Y. Liu, Y. Shi, D. Zhang, J. Li, G. Huang, *Polymer* **2013**, *54*, 6140.
[55] A. Tasić, M. Pergal, M. Antić, V. Antić, *J. Serb. Chem. Soc.* **2017**, *82*, 1395.
[56] Q. Zhang, Y. Yang, D. Suo, S. Zhao, J. C.-W. Cheung, P. H.-M. Leung, X. Zhao, *ACS Nano* **2023**, *17*, 16798.
[57] Y. Zhang, X. Zhang, Y.-Q. Zhao, X.-Y. Zhang, X. Ding, X. Ding, B. Yu, S. Duan, F.-J. Xu, *Biomater. Sci.* **2020**, *8*, 997.
[58] C. R. Thornton, *Advances in Applied Microbiology*, (Eds: G.M. Gadd, S. Sariaslani), Academic Press, Philadelphia, USA **2020**, pp. 1–61.
[59] G. W. Gooday, *Mycological Research* **1995**, *99*, 385.
[60] H. Yu, L. Wang, Z. Zhang, X. Zhang, S. Luan, H. Shi, *Adv. Healthcare Mater.* **2023**, *12*, 2202096.
[61] Y. Zhang, J. Cui, K.-Y. Chen, S. H. Kuo, J. Sharma, R. Bhatta, Z. Liu, A. Ellis-Mohr, F. An, J. Li, Q. Chen, K. D. Foss, H. Wang, Y. Li, A. M. McCoy, G. W. Lau, Q. Cao, *Sci. Adv.* **2023**, *9*, eadg7397.
[62] Q. Zeng, Y. Zhu, B. Yu, Y. Sun, X. Ding, C. Xu, Y.-W. Wu, Z. Tang, F.-J. Xu, *Biomacromolecules* **2018**, *19*, 2805.
[63] Q. Song, Z. Xiao, T. Liu, H. Gao, X. Chen, Q. Jia, P. Li, D. Wei, *ACS Macro Lett.* **2024**, *13*, 1056.
[64] A. Genest, S. Binauld, E. Pouget, F. Ganachaud, E. Fleury, D. Portinha, *Polym. Chem.* **2017**, *8*, 624.
[65] A. Genest, D. Portinha, E. Fleury, F. Ganachaud, *Prog. Polym. Sci.* **2017**, *72*, 61.
[66] J. Xu, Z. Xie, F. Du, X. Wang, *J. Mater. Sci. Technol.* **2021**, *69*, 79.
[67] J. Liang, J. She, H. He, Z. Fan, S. Chen, J. Li, B. Liu, *Appl. Surf. Sci.* **2019**, *478*, 770.
[68] S. Chen, S. Zhang, M. Galluzzi, F. Li, X. Zhang, X. Yang, X. Liu, X. Cai, X. Zhu, B. Du, J. Li, P. Huang, *Chem. Eng. J.* **2019**, *358*, 634.
[69] J. Li, P. Zhang, M. Yang, Z. Xie, G. Li, X. Wang, *ACS Appl. Polym. Mater.* **2022**, *4*, 1922.
[70] C. Chen, Z. Xie, P. Zhang, Y. Liu, X. Wang, *Colloid Interface Sci. Commun.* **2021**, *40*, 100336.
[71] P. Zhang, J. Li, M. Yang, L. Huang, F. Bu, Z. Xie, G. Li, X. Wang, *ACS Biomater. Sci. Eng.* **2022**, *8*, 570.
[72] P. Zhang, M. Yang, J. Li, Z. Xie, G. Li, X. Wang, *Colloid Interface Sci. Commun.* **2022**, *46*, 100567.
[73] W. Chu, Y. Ma, Y. Zhang, X. Cao, Z. Shi, Y. Liu, X. Ding, *Colloids Surf., B* **2023**, *222*, 112979.
[74] F. Du, A. Wenjing, F. Liu, B. Wu, Y. Liu, W. Zheng, W. Feng, G. Li, X. Wang, *Carbohydr. Polym.* **2023**, *316*, 121058.
[75] Y. Su, Z. Zhi, Q. Gao, M. Xie, M. Yu, B. Lei, P. Li, P. X. Ma, *Adv. Healthcare Mater.* **2017**, *6*, 1601173.
[76] Y. Hu, Y. Qiao, P. Lei, Y. Gu, L. Sun, Y. Qiu, S. Li, H. Xu, R. Wang, *Chem. Eng. J.* **2023**, *474*, 145502.